Structure
Article

The Modular Structure of the Inner-Membrane Ring Component PrgK Facilitates Assembly of the Type III Secretion System Basal Body

Julien R.C. Bergeron,[1,2] Liam J. Worrall,[1,2] Soumya De,[1] Nikolaos G. Sgourakis,[3] Adrienne H. Cheung,[1] Emilie Lameignere,[1,2] Mark Okon,[1] Gregory A. Wasney,[1,2] David Baker,[4] Lawrence P. McIntosh,[1,5] and Natalie C.J. Strynadka[1,2,*]

[1]Department of Biochemistry and Molecular Biology, The University of British Columbia, 2350 Health Sciences Mall, Vancouver, BC, V6T 1Z3, Canada
[2]Centre for Blood Research, University of British Columbia, 2350 Health Sciences Mall, Vancouver, BC, V6T 1Z3, Canada
[3]National Institute of Diabetes & Digestive & Kidney Diseases, National Institutes of Health, 9000 Rockville Pike, Bethesda, MD 20892, USA
[4]Department of Biochemistry, Department of Genome Sciences, and Howard Hughes Medical Institute, University of Washington, 4000 15th Avenue NE, Seattle, WA 98195, USA
[5]Department of Chemistry, University of British Columbia, 2350 Health Sciences Mall, Vancouver BC, V6T 1Z3, Canada
*Correspondence: ncjs@mail.ubc.ca
http://dx.doi.org/10.1016/j.str.2014.10.021

SUMMARY

The type III secretion system (T3SS) is a large macromolecular assembly found at the surface of many pathogenic Gram-negative bacteria. Its role is to inject toxic "effector" proteins into the cells of infected organisms. The molecular details of the assembly of this large, multimembrane-spanning complex remain poorly understood. Here, we report structural, biochemical, and functional analyses of PrgK, an inner-membrane component of the prototypical *Salmonella typhimurium* T3SS. We have obtained the atomic structures of the two ring building globular domains and show that the C-terminal transmembrane helix is not essential for assembly and secretion. We also demonstrate that structural rearrangement of the two PrgK globular domains, driven by an interconnecting linker region, may promote oligomerization into ring structures. Finally, we used electron microscopy-guided symmetry modeling to propose a structural model for the intimately associated PrgH-PrgK ring interaction within the assembled basal body.

INTRODUCTION

Salmonella is a Gram-negative bacterium, several strains of which are human pathogens. *S. typhimurium* is a major source of food-borne enterocolitis, whereas *S. typhi* is the etiological agent for typhoid fever, a disease that remains endemic in the developing world (Haraga et al., 2008). A common feature of all pathogenic strains of *Salmonella* is the presence of *Salmonella* Pathogenicity Islands (SPIs) in their genome. Specifically, two of these (SPI-1 and SPI-2) encode for type III secretion systems (T3SS), large macromolecular assemblies responsible for the injection of toxic "effector" proteins into the cytosol of infected cells (Coburn et al., 2007a; de Jong et al., 2012). T3SSs have been identified as essential pathogenicity components in many infectious Gram-negative bacteria, including *Salmonella* spp., enteropathogenic *E. coli* (EPEC) and enterohemorrhagic *E. coli*, *Pseudomonas aeruginosa*, *Yersinia* spp., *Shigella* spp., *Chlamydia* spp., and *Vibrio* spp. (Coburn et al., 2007b; Troisfontaines and Cornelis, 2005). This renders the T3SS a very attractive target for the development of new antibiotics and vaccines (Keyser et al., 2008; Kline et al., 2012; Marshall and Finlay, 2014).

A T3SS consists of a series of conserved genes coding for the secretion apparatus ("injectisome") and of a set of genes coding for the effector proteins, which vary between systems and species (Büttner, 2012; Kosarewicz et al., 2012). Effector proteins are channeled through the injectisome to the cytosol of target cells (Dohlich et al., 2014; Radics et al., 2014). A number of groups have employed an integrative approach (Alber et al., 2008) to obtain structural models of the prototypical *Salmonella* SPI-1 T3SS injectisome. Electron microscopy (EM) studies have revealed its global organization (Marlovits et al., 2004; Schraidt et al., 2010; Schraidt and Marlovits, 2011), and the atomic structures of several isolated domains have been reported (Bergeron et al., 2013; Lunelli et al., 2011; Spreter et al., 2009; Wang et al., 2007). Cross-linking in combination with mass spectrometry was employed to obtain information on the interaction between the various components (Sanowar et al., 2009; Schraidt et al., 2010). Finally, computational methods have been developed to combine these data in order to obtain an atomic model of the T3SS injectisome architecture (Bergeron et al., 2013; Demers et al., 2013).

However, the mechanistic details for the assembly of this large complex (~3.5 MDa) remain poorly understood. Genetic, biochemical, and EM data have demonstrated that the inner-membrane components of the injectisome can assemble independently, with the proteins PrgK and PrgH (Figure 1A) forming intimately nested 24-mer ring structures around the inner-membrane components SpaPQRS (Kimbrough and Miller, 2000; Wagner et al., 2010). Biochemical data also showed that in parallel the secretin InvG forms a pore in the outer membrane (Figure 1A), facilitated by the action of the pilotin lipoprotein InvH

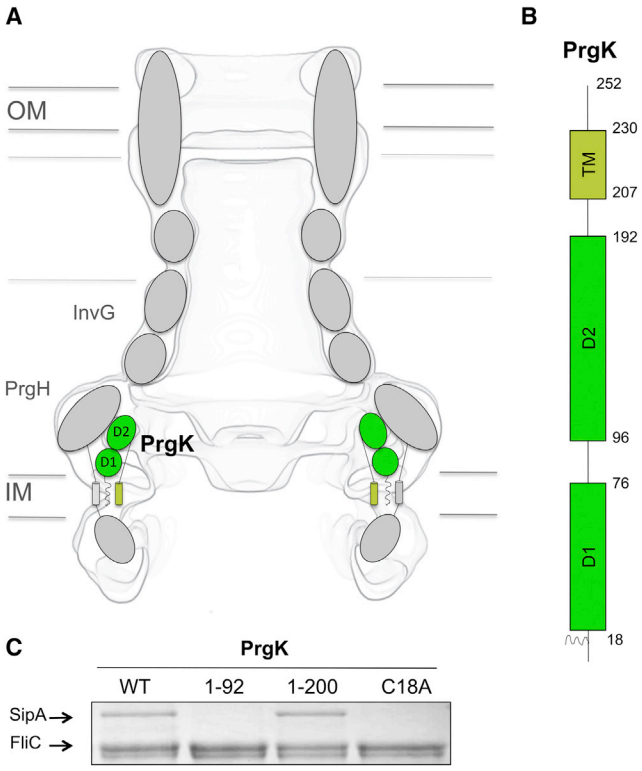

Figure 1. PrgK Arrangement and Localization in the T3SS Basal Body

(A) Schematic representation of the major ring proteins that form the *Salmonella* SPI-1 T3SS basal body within the context of the EM map used in this study (EMD-1875). The localization of the various domains of PrgK is shown in green.

(B) The PrgK D1 and D2 domain boundaries are indicated, as well as positions of the putative lipidation site at Cys 18 (indicated by a squiggly line) and the TM helix.

(C) SDS-PAGE gel of proteins secreted by *S. typhimurium* strains containing mutations of PrgK's putative membrane-embedded domains. The flagellar protein FliC is used as an internal loading control. SipA is secreted when PrgK is expressed and with the deletion of the C-terminal TM helix ($PrgK_{1–200}$). Secretion is abrogated with the deletion of D2 ($PrgK_{1–92}$) and when the proposed lipidation site is mutated (C18A).

See also Figure S1.

(Crago and Koronakis, 1998; Okon et al., 2008; Spreter et al., 2009). The inner-membrane and outer-membrane components are proposed to come together through interactions of their periplasmic domains and to then recruit the cytoplasmic ATPase complex, leading to a secretion-competent complex (Sanowar et al., 2009; Schraidt et al., 2010).

In this study, we use structural, biochemical, and functional methods to investigate the assembly of the prototypical *Salmonella* SPI-1 T3SS inner-membrane component, PrgK. We report the structures of its two globular domains, and we use computational methods to propose a model for the PrgK-PrgH interaction in the assembled basal body (the major T3SS injectisome subcomplex isolated from bacteria and composed largely of the inner and outer membrane ring components PrgH, PrgK, and InvG; see Figure 1A). This model suggests that each PrgH monomer docks in between adjacent PrgK subunits. We also show that a linker region of PrgK may regulate oligomerization through multiple interactions with the flanking globular domains. Based on these results, we propose a molecular model for the stepwise assembly of the PrgK-PrgH inner-membrane ring.

RESULTS

Elucidating the Roles of PrgK's Membrane-Embedded Domains

PrgK is an inner-membrane component of the *Salmonella* SPI-1 T3SS basal body (Kimbrough and Miller, 2000) (Figure 1A). At its N terminus, PrgK possesses a canonical lipoprotein signal sequence, with a conserved cysteine residue (Cys 18) forming a predicted site of lipidation (Juncker et al., 2003). Lipidation has been experimentally confirmed in vivo for the closely related *Shigella* ortholog MxiJ (44% sequence identity) (Allaoui et al., 1992). In addition, a C-terminal transmembrane (TM) helix is predicted in all PrgK orthologs, except the EPEC T3SS component EscJ (Figure 1B; Figure S1A available online). Nanogold labeling experiments have shown that the C terminus of PrgK is located in the cytoplasm, confirming that PrgK traverses the inner membrane (Schraidt et al., 2010).

To assess the role of the putative N-terminal lipidation and C-terminal TM helix for basal body assembly, we monitored secretion of effector proteins in a *S. typhimurium* strain containing a chromosomal deletion of the *prgK* gene and complemented with plasmids encoding WT *prgK* or mutants. Surprisingly, removal of the C-terminal 52 residues, which include the cytoplasmic tail and TM helix ($PrgK_{1–200}$), does not alter effector secretion (Figure 1C). This observation demonstrates that the TM helix of PrgK is not essential for inner-membrane localization or basal body assembly. In contrast, secretion is abrogated when the putative N-terminal lipidation site is mutated (C18A), suggesting a requirement for the specific anchoring of PrgK to the inner membrane via lipidation of Cys 18.

Following from the above observations, we were able to purify intact needle complexes from *Salmonella* strains lacking the TM helix of PrgK, as observed by negative-stain EM (Figures S1B and S1C). We note that the yield of complexes obtained with the $PrgK_{1–200}$ truncation is approximately 10-fold lower than with the WT PrgK. This suggests that the TM helix does contribute to the overall stability of the needle complex.

Structures of the PrgK Globular Domains

Existing homology models of the PrgK ring structure (Sanowar et al., 2009; Schraidt and Marlovits, 2011; Worrall et al., 2011) are based on the experimental observation of a superhelical array of 24-mer containing successive turns found in the crystal structure of the EPEC ortholog, EscJ (26% identity) (Yip et al., 2005). However, we showed previously that ring models of basal body domains based on the structures of distant homologs lead to inaccuracies, including domain misorientation and clashes, and interfered with model convergence in our EM-guided symmetry modeling procedure (Bergeron et al., 2013). Therefore, in order to obtain a more accurate PrgK ring model, the experimentally determined structure of the PrgK monomer was required. To this end, we expressed a recombinant construct of its periplasmic domain lacking the lipidation site ($PrgK_{19–200}$). This protein

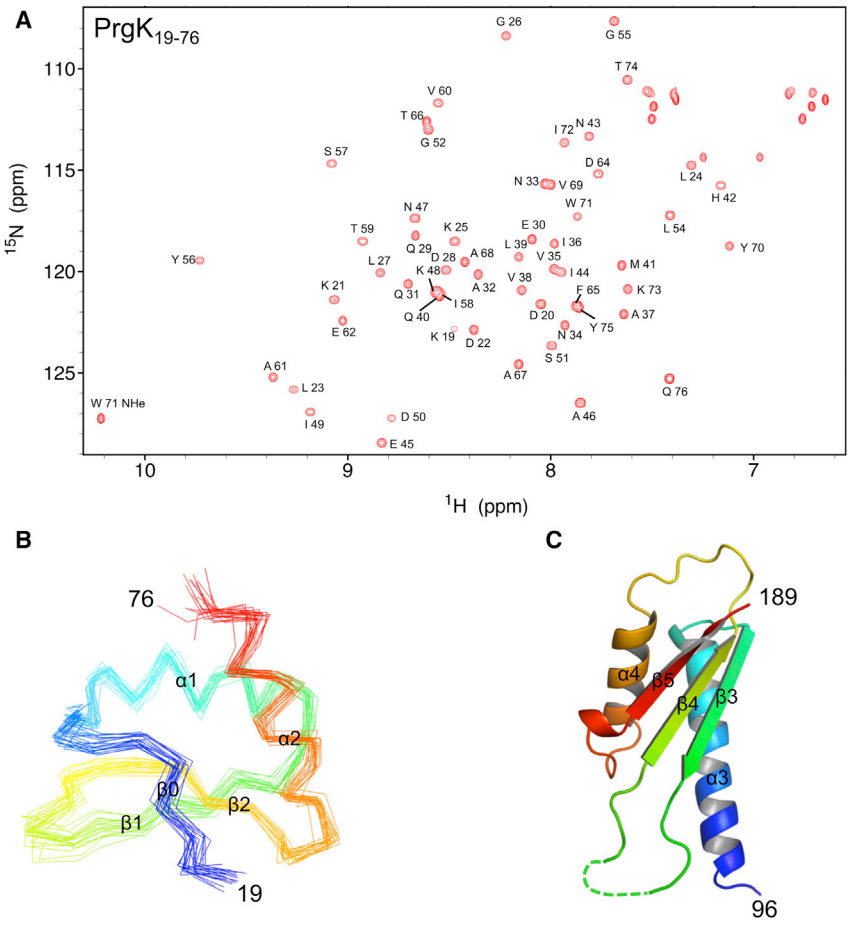

Figure 2. Structure of the Two PrgK Globular Domains

(A) ^{15}N-HSQC spectrum of PrgK $_{D1}$, with the assigned residues indicated.

(B) Overlay of the 20 lowest energy members in the NMR-derived structural ensemble of PrgK D1, with only the backbone trace represented.

(C) X-ray crystallographic structure of PrgK D2, in a ribbon representation, with corresponding sequence numbering shown. Dashed line indicates residues not resolved in the electron density. For (B) and (C), secondary structure elements are labeled as in Figure S1A, and blue to red rainbow coloring indicates N- to C-terminal directionality.

See Tables 1 and 2 for statistics and also Figure S2.

could be purified to high yield, but underwent proteolytic degradation at 20°C (hours) and 4°C (days), leading to two products of approximately 14 and 9 kDa size, respectively (data not shown). Crystal and solution structures of EPEC EscJ (Crepin et al., 2005; Yip et al., 2005) have revealed that this homologous protein possesses two globular domains (7 and 10 kDa) joined by an extended linker (Figures 1B and S1A). We therefore purified the two corresponding globular domains of PrgK independently. We could not obtain crystals for the N-terminal domain (PrgK$_{19–76}$, henceforth referred to as D1). However, this protein yielded high-quality nuclear magnetic resonance (NMR) spectra (Figure 2A), allowing us to solve its solution structure (Figure 2B; Table 1). Further, we were successful in obtaining crystals of the C-terminal domain (PrgK$_{98–200}$, henceforth D2) and could solve its structure by X-ray crystallography (Figure 2C; Table 2; see Supplemental Experimental Procedures for details).

The folds of the PrgK D1 and D2 domains are similar to those of the equivalent domains in the EPEC T3SS ortholog EscJ (Figure S2), with backbone RMS deviations <1.5 Å. Both D1 and D2 possess the canonical ring-building motifs observed in other components of the T3SS basal body (Bergeron et al., 2013; Spreter et al., 2009). We note that the first strand (termed β0 here for consistency) of EscJ D1 is not observed in PrgK, possibly due to a single residue insertion at position 23 based on the sequence alignment (Figure S1A), which either destabilizes or prevents its formation. In addition, PrgK D2 possesses a six-residue insertion (from 136–141) in a loop region between strands β3 and β4 relative to EscJ (Figures S1A and S2). This insertion is only partially ordered in the PrgK D2 crystal structure (Figures 2C and S2; see Supplemental Experimental Procedures for details).

Modeling of the PrgK 24-mer Ring

We next applied our NMR and crystallographic structures to an EM-guided symmetry modeling protocol (Bergeron et al., 2013) to model the PrgK 24-mer ring oligomer. Starting from the monomeric structures of D1 and D2, we applied the procedure to the two domains independently (Figure S3; Supplemental Experimental Procedures for details), allowing us to obtain a refined model for PrgK (Figure 3A). Notably, despite this independent starting set, the final model is globally similar in intermolecular packing to the intact EscJ ring model derived from the crystallographically determined superhelical structure (Figures S3C and S3D), with both domains in each of these orthologs adopting similar orientations. We further note that the diameter of the D2 ring is larger in the PrgK model, in agreement with the dimension of the region of density assigned to PrgK in the EM map. It has been reported that the EPEC T3SS possesses a narrower basal body compared with the *Salmonella* SPI-1 T3SS (Sekiya et al., 2001), suggesting that the larger PrgK D2 ring may correspond to structural differences between the two systems.

We then observed that in the Rosetta-based PrgK model, the D1 and D2 domains are in close proximity, forming a number of notable direct interactions, including between residues 70–75 at the surface of helix α2 of D1, and residues 111–126 on α4 and strand β3 of D2 (Figure 3B). This prompted us to investigate whether the D1 and D2 domains of PrgK interact in vitro. Using NMR spectroscopy, we monitored spectral perturbations in the ^{15}N-labeled D1 domain upon titration with unlabeled D2. As shown in Figure 3C, we could observe a number of amide ^{1}H-^{15}N with progressively perturbed chemical shifts, implicating residues 70–74 of helix α2, and to a lesser extent, those in the spatially adjacent helix α1 (residues 38–42). These are largely hydrophobic residues, which cluster on the surface of D1 formed

Table 1. NMR and Refinement Statistics for the PrgK D1 Structure

	$PrgK_{19–76}$
NMR Distance and Dihedral Constraints	
Distance constraints	
Total NOE	1,912
Intraresidue	147
Interresidue	
Sequential ($\|i-j\|=1$)	1,197
Medium range ($\|i-j\|<4$)	296
Long range ($\|i-j\|>5$)	272
Hydrogen bonds	20
Total dihedral angle restraints	
ϕ	50
ψ	51
Structure Statistics	
Violations (means ± SD)	
Distance constraint violation (Å)	0.013 ± 0.0003
Dihedral angle violation (°)	0.716 ± 0.0197
Deviations from idealized geometry	
Bond lengths (Å)	0.004
Bond angles (°)	0.6
Impropers (°)	0
Average pairwise root-mean-square deviation[a] (Å)	
Heavy	1.15 ± 0.11
Backbone	0.63 ± 0.09

[a]Pairwise root-mean-square deviation was calculated among 20 refined structures.

Table 2. Data Collection and Refinement Statistics for the PrgK D2- and D1-linker Structures

	$PrgK_{96–200}$	$PrgK_{19–92}$
Data Collection		
Space group	C2	$P2_12_12$
Cell dimensions		
a, *b*, *c* (Å)	77.19 34.74 64.03	88.12 112.10 112.10
α, β, γ (°)	90.00 110.76 90.00	90.00 90.00 90.00
Resolution (Å)	2.60 (2.7–2.6)	3.20 (3.37–3.20)
R_{sym}	0.071 (0.420)	0.165 (0.387)
$I/\sigma I$	9.6 (2.1)	4.2 (2.1)
Completeness (%)	99.3 (94.2)	100.0 (100.0)
Redundancy	3.7 (3.6)	7.4 (7.5)
Refinement		
Resolution (Å)	2.6	3.2
Number of reflections	4992	17949
R_{work}/R_{free}	0.227/0.259	0.2468/0.2764
Number of atoms	1,344	6,912
Protein	1,337	6,912
Ligand/ion	0	0
Water	7	0
B factors (Å^2)		
Protein	48.7	43.00
Water	45.2	N/A
Root-mean-square deviation		
Bond lengths (Å)	0.009	0.011
Bond angles (°)	1.09	1.85

Values in parentheses are for highest resolution shell.

by the two helices of the domain (Figure 3D) and match with the interface generated in the PrgK 24-mer model (Figure 3B). In parallel, a weak endothermic reaction was observed when we used isothermal titration calorimetry (ITC) to monitor the titration of D1 against D2 (Figure 3E). However, over the available concentration range, we were unable to saturate the ITC- and NMR-monitored titration, indicating that it is a weak interaction with an affinity likely in the millimolar range (Figure 3C). Nevertheless, this interaction is specific, as evidenced by its abrogation when Tyr70 (a residue in helix α2 that is perturbed in the NMR titrations; Figure 3C) is mutated to Ala (Figure 3E). Collectively, these experiments both confirm that the isolated D1 and D2 domains do interact and identify the D1 α1-α2 surface as the primary constituent of the D1-D2 interface (Figure 3D). Importantly, this matches the interface generated in the PrgK 24-mer model (Figure 3B). We emphasize that that the weak intermolecular interaction of the isolated D1 and D2 is not unexpected given that the two are removed from their native intramolecular arrangement. In addition, cooperativity within the 24-mer may "amplify" the interaction.

The Linker Region of PrgK Promotes Oligomerization

We further noted that the residues involved in the D1-D2 interaction identified in PrgK (Figure 3) are also present in the EscJ superhelix crystal structure (Figure 4A). However, in the latter, we observed that this interaction occurs between adjacent molecules, with D1 of molecule i interacting with D2 of molecule i+1 along the 24-mer oligomeric ring (we refer to this arrangement as a "domain-swapped" conformation). This is likely driven by the linker region, which is well ordered and forms a number of interactions with D2 (Figure 4B), but not with D1 or with linker regions from adjacent molecules. As we have modeled the two domains D1 and D2 of PrgK independently, we cannot directly distinguish whether the analogous D1-D2 interaction occurs in an intermolecular domain-swapped conformation (Figure 4C, right), as opposed to an intramolecular interaction between domains within a single chain (Figure 4C, left).

To answer this question, we engineered a construct of PrgK D2 containing the upstream linker region ($PrgK_{82–200}$). Unexpectedly, we observed that this protein forms a large homo-oligomeric complex, as shown using size-exclusion chromatography with multiangle light scattering (SEC-MALS) (Figure 5A, brown curve), whereas in the absence of the linker, D2 is monomeric (purple curve). Importantly, the fold of D2 is likely globally conserved in the $PrgK_{82–200}$ construct, as shown by CD spectroscopy (Figure S4A), supporting that this oligomer is not constituted of unstructured, aggregated protein. A closer analysis of the EscJ superhelix structure revealed that a conserved Phe at position 89 in the linker region docks into a hydrophobic pocket formed by two adjacent D2 subunits (Figure 5B). We therefore

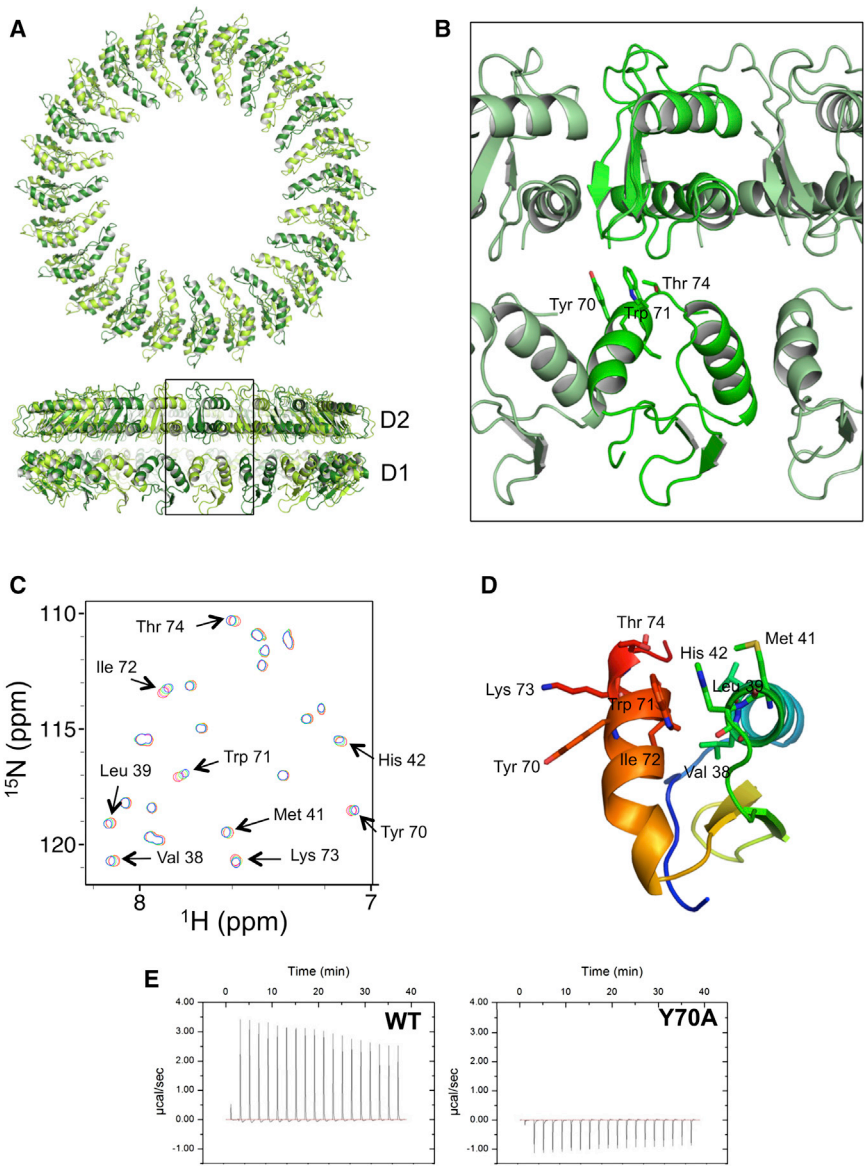

Figure 3. Modeling of the PrgK Ring

(A) Ribbon representation of the PrgK D1 and PrgK D2 ring models in the relative orientation that they adopt in the EM map density of the needle complex used for modeling (see Supplemental Experimental Procedures for details).

(B) Expanded view of adjacent D1 and D2 molecules in the ring model. Residues of D1 that form hydrophobic interactions with D2 are shown in sticks.

(C) Section of the overlaid ^{15}N-HSQC spectra of PrgK D1 alone (red) and with increasing amount of unlabeled D2 (up to 2:1 ratio for D2:D1, in the blue spectrum). The residues experiencing a significant chemical shift perturbation are indicated.

(D) These residues are shown in sticks on the D1 structure and clearly match with residues that form contacts with D2 in (B).

(E) ITC isotherms for the titration of PrgK D1 against PrgK D2. A weak (mM range) endothermic interaction is observed between D1 and D2 (left), which is disrupted when the Y70A mutation is introduced to D1 (right).

See also Figure S3.

hypothesized that this residue may also stabilize the PrgK$_{82–200}$ oligomer. Indeed, we observed that a mutation of Phe89 to Ala abrogates the oligomerization of PrgK$_{82–200}$ (Figure 5A, green curve) in vitro, confirming that the linker promotes D2 oligomerization in a similar fashion to that observed in the EscJ superhelix structure. We note that this mutation does not compromise T3SS secretion in vivo, nor does the Y70A mutation (which disrupts the oligomeric interaction between D1 and D2, see above). However, the double-mutant F89A/Y70A does abrogate secretion (Figure S4C), which suggests that PrgK oligomerization is likely stabilized by a number of interactions, including those involving residues Phe89 and Tyr70. The NMR spectrum of PrgK$_{19–200}$ with the Y70A/F89A mutations (Figure S4D) confirmed that the overall fold of the protein is conserved, and its stability was confirmed by differential fluorescence calorimetry (Figure S4B). Further structural characterization of this protein was not possible due to its propensity to undergo degradation (see above).

Finally, we used negative-stain EM to analyze the PrgK$_{82–200}$ oligomer and observed that it forms ring-shaped/tubular structures, with a conserved diameter of ~15–20 nm (Figure 5C). This diameter is similar to that observed in both the EscJ superhelix structure (Yip et al., 2005) and in the density attributed to the PrgK ring in the high-resolution cryo-EM map of the basal body (Schraidt and Marlovits, 2011). However, the structures vary in length from a few nm to over 100 nm (Figure 5C). Based on these observations, we propose that these filaments consist of a superhelical assembly of PrgK D2, which putatively forms in the absence of the membrane-embedded N-terminal lipidation that would restrict its assembly to a 2D plane. We note that the heterogeneous nature of these structures prevented any high-resolution characterization, as would be required to formally demonstrate their biological significance.

From these results, we conclude that in the EPEC EscJ and *Salmonella* PrgK inner-membrane rings D1 and D2 likely form a domain-swapped interface between adjacent molecules. We hypothesize that this allows for a more extensive set of interactions within the 24-mer rings, including with the linker region, to promote oligomerization.

Interaction between D1 and Linker Prevents Oligomerization

We have demonstrated that the linker is sufficient to promote oligomerization of D2 in vitro, in the absence of D1. However, no oligomerization was observed for the PrgK$_{19–200}$ construct, which includes D1, D2, and the linker (Figure 5A, blue curve). This suggested the possibility that D1 may prevent spontaneous

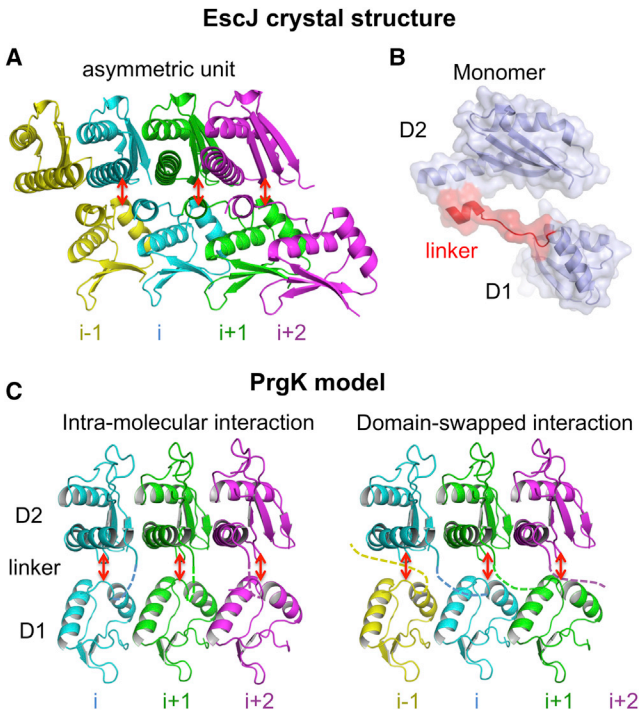

Figure 4. D1 and D2 Form an Intermolecular Interaction in the Assembled 24 Mer

(A) Ribbon representation of an asymmetric unit from the EscJ crystal structure containing four adjacent molecules in the superhelix (PDB ID: 1YJ7). Chains are colored in yellow (chain i-1), cyan (chain i), green (i+1), and magenta (i+2).

(B) Ribbon and surface representation of one monomer from the EscJ superhelix crystal structure, with the linker region shown in red. It is largely ordered, with only four residues not resolved in the electron-density map. Residues 86–89 form a short helix, which interacts with D2.

(C) Ribbon representation of successive molecules in our PrgK D1 and D2 model, colored as in (A). Two possible chain assignments can be made: interacting D1 and D2 domains can belong to the same chain and form intramolecular interaction identified with red arrows (left) or belong to adjacent chains and form a domain-swapped interaction (right). EscJ exhibits the latter, whereas in our PrgK model these two conformations are indistinguishable, as the linker (shown here with a dashed line) was not modeled.

and potentially premature oligomerization of PrgK in the inner membrane.

To validate this hypothesis, we engineered a protein construct including D1 followed by the linker region ($PrgK_{19–92}$). Using ITC, we observed that the D1-D2 interaction is abrogated in the context of the D1-linker construct (Figure 6A). To understand how the presence of the linker residues abrogates this interaction, we used NMR spectroscopy to characterize $PrgK_{19–92}$ further. Unexpectedly, we observed that many residues yield two distinct sets of NMR signals (Figure 6B), indicative of two conformations in slow exchange, referred to as "population A" and "population B," with the peaks yielded by population A consistently more intense than those yielded by population B. We mapped chemical shift differences between these two populations along the sequence, which inferred that structural differences occur primarily in the α helices and the following linker (Figure 6C). However, the chemical shift-derived secondary structure prediction suggests that population A and population B possess similar secondary structure elements. The Random Coil Index (Berjanskii and Wishart, 2007) also reveals that residues 70–82 (end of helix 2 and beginning of the linker) are less flexible in population A than in population B (Figure 6C). We note that most peaks found in the spectrum of PrgK D1 overlay onto the peaks assigned to population B of $PrgK_{19–92}$ (Figure S5A), indicating that in population B the linker does not interact significantly with the D1 domain. These results suggest that in population A, residues 76–82 of the linker interact with D1, while this interaction is not present in population B. Importantly, the spectrum of $PrgK_{19–92}$ overlay well onto that of the construct that included both PrgK domains ($PrgK_{19–200}$; Figure S5B), with the two peaks formed by population A and population B clearly observable in the larger construct. This demonstrates that the interaction between D1 and the linker is also present in the purified, monomeric full-length protein (lacking the N-terminal lipidation site and C-terminal TM region), which could not be characterized further due to its instability (see above).

Next, we were able to solve the crystal structure of $PrgK_{19–92}$ (Figure 6D; Table 2; see Supplemental Experimental Procedures for details). In this structure, part of the linker (residues 75–82) is well ordered and clearly located in the D2-binding groove of D1, in agreement with the NMR results described above. Notably Tyr 75, Leu 77, and Pro 78 form hydrophobic interactions with loop 1, helix α1, and helix α2 of D1 (Figure 6E). We note that only the linker-bound conformation, corresponding to population A, was found in the crystal. It is also noteworthy that this protein forms a superhelical arrangement in the crystal lattice, in which intermolecular contacts supports the D1 ring model reported above (Figures S5C and S5D). Together, these results demonstrate that D1 interacts with the linker, through the groove formed in between the two helices of the domain. This corresponds to the surface of D1 that interacts with D2, as shown by our modeling and NMR results (see Figures 6C and 3D). From this observation, we conclude that the linker interacts with the D2 binding pocket of D1, thereby sterically blocking the D1-D2 interaction. Furthermore, by sequestering the linker, D1 likely also prevents spontaneous oligomerization of PrgK.

To provide additional support for this hypothesis, we used NMR spectroscopy to monitor the titration of PrgK D1 with an isolated polypeptide corresponding to the linker sequence ($PrgK_{76–97}$) fused to SUMO. As summarized in Figure S5E, a number of D1 residues showed amide chemical shift changes upon peptide addition. These residues clustered around the helical regions of D1 (Figure S5G). This confirms that the linker binds the same region of D1, whether present as a separate peptide or in the intramolecular context of $PrgK_{19–92}$. Furthermore, chemical shift analysis (Figure S5F) allowed us to obtain a K_d value of 100 μM ($\pm$40 μM) for the intermolecular D1-linker interaction. This is at least an order of magnitude tighter than the intermolecular D1-D2 interaction. The preferential D1-linker interaction is consistent with the observations by NMR and SEC-MALS that $PrgK_{19–200}$ is monomeric.

Structural Basis for the PrgH-PrgK Interaction

We next combined the 24-mer models of PrgK D1 and D2 described above (Figure 3A), with the PrgH oligomeric model reported previously (Bergeron et al., 2013), and applied the ring

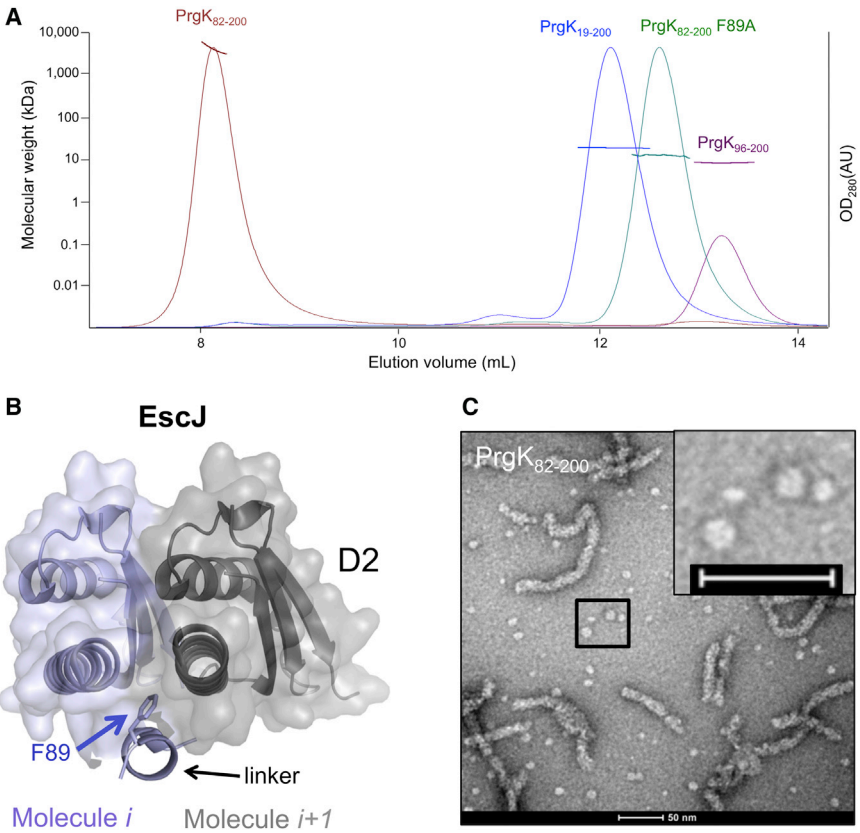

Figure 5. The Linker Promotes PrgK D2 Oligomerization

(A) SEC-MALS analysis of the PrgK D2 constructs, with the elution volume from a Superdex 200 column on the x axis, and the calculated molecular mass along the y axis. $PrgK_{82–200}$ forms a large oligomeric structure (brown) with molecular weight varying from 1.5 to 10 MDa, whereas $PrgK_{96–200}$ is monomeric, with a measured molecular mass of 10.5 kDa (purple). Oligomerization of $PrgK_{82–200}$ is abrogated by the F89A mutation, which is monomeric with a measured molecular weight of 15.2 kDa (green). Finally, the full-length protein, containing D1, the linker and D2, is strictly monomeric, with a measured molecular weight of 22.6 kDa (blue), suggesting that D1 abrogates the linker-induced oligomerization of D2.

(B) Domain D2 of two adjacent molecules in the EscJ crystal structure (PDB ID: 1YJ7) (Yip et al., 2005) are shown in ribbon and surface representation, with the linker region of molecule i shown in ribbon. The position of Phe 89, which promotes oligomerization in $PrgK_{82–200}$, is shown with a blue arrow.

(C) Negative-stain EM analysis of purified $PrgK_{82–200}$ protein, showing large tubular assemblies of constant diameter but varying lengths. Individual ring structures, with dimensions that are consistent with EscJ 24-mers, are shown at closer magnification on the top right.

See also Figure S4.

modeling procedure on the collective set (see Figures S6A and S6B; Supplemental Experimental Procedures for details). From this we obtained a model for the PrgH-PrgK 48-mer ring complex (Figure 7A), which agrees with the EM map (Figure S6C), and previously published biochemical data (Table S1). We emphasize that the model includes a number of assumptions, such that the subunits are related by strict symmetry, and that the structures of individual domains are not significantly modified in the assembled complex. Higher resolution EM maps, crystal structures of oligomerized domains, and additional mass spectrometry/crosslinking and mutagenesis interaction data should allow for generation of models with greater accuracy in the future. In particular, while the agreement with the NMR titration and EscJ crystallographic contacts supports the PrgK model, additional experimental restraints would be necessary to better define the PrgH-PrgK interaction.

In this model, we observe that there are predicted contacts between the periplasmic domains of PrgH and PrgK monomers (Figure 7B). However, this intermolecular interface is relatively limited (collectively 1,440 $Å^3$ of buried surface for the modeled complex) and with the major interactions occurring between the C-terminal region of PrgH and PrgK D2. This is in agreement with the highest resolution (~10 Å) EM map (Schraidt and Marlovits, 2011), in which a large cavity is observed between the sections of the density attributed to PrgH and PrgK (Figure 7B). Specifically, in the PrgH-PrgK model, the conserved Asp 333 (located on helix 2 in the third ring-building motif domain of PrgH) is buried in a well-ordered, positively charged pocket formed by helix α4 of two adjacent PrgK D2 subunits (Figure 7C). Consistent with this arrangement, we were not able to detect an interaction between the periplasmic domain of PrgH and PrgK in vitro (data not shown), likely because this construct does not form the PrgH binding pocket in its monomeric state. The highly oligomeric and heterogeneous state of the $PrgK_{82–200}$ construct did not allow for further investigation of its interaction with PrgH. As shown in Figure 7D, mutation of Asp 333 to Arg in PrgH abrogates secretion (without affecting the structure of the isolated domain; Figures S6D and S6E), supporting the essential role of this residue. In PrgK, mutation of the conserved Lys 168 to Glu does not alter secretion, but it is abrogated when both Lys 168 and Arg 169 are mutated to Ala. CD spectroscopy and differential scanning calorimetry (DSF) suggest that PrgK D2 is largely folded in the presence of these mutations (Figures S6F and S6G). We also observe that the loop located between strand β5 and helix α5 of D2, which is poorly ordered in the PrgK crystal structure (see Supplemental Experimental Procedures), is located in the cavity described above (Figure 7B) in our PrgK ring model. Neither this loop nor the extended loop between strands β4 and β5 is accounted for by EM map density. It is therefore possible that flexible regions of PrgK could potentially form additional contacts with PrgH upon complex formation.

DISCUSSION

In this study, we characterize structural and functional features of the modular ring building domains of the inner-membrane

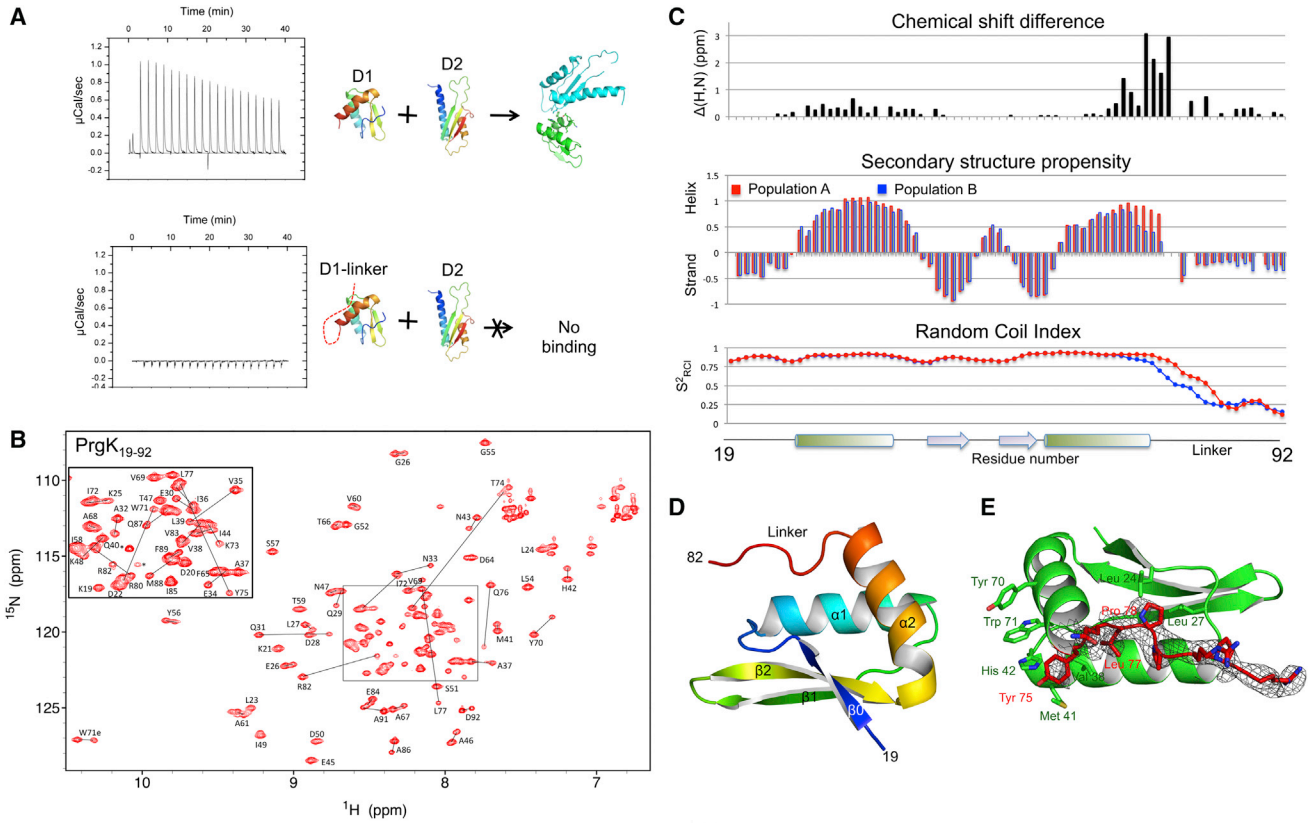

Figure 6. D1 Sequesters the Linker to Prevent Oligomerization

(A) ITC isotherms for the titration of PrgK D1 against D2. A schematic representation of the experiments performed is shown on the right. In the presence of the linker region fused to D1 ($PrgK_{19–92}$), the two domains do not interact. The top is a repeat of the experiment shown on Figure 3E (left).

(B) Assigned ^{15}N-HSQC spectrum of $PrgK_{19–92}$ (insert for the crowded region). Black lines connect peaks arising from the same residue in the two populations (A and B) of this protein. The asterisk indicates peaks assigned to the two cloning remnant residues at the N terminus of the PrgK sequence.

(C) The weighted combined amide ^{15}N and $^{1}H^{N}$ chemical shift differences (Δ(H,N)) between corresponding peaks for population A and population B is plotted along the protein sequence (top). The perturbed amides cluster in helices α1, α2 and the linker region. Secondary structures for the populations A and B of $PrgK_{19–92}$, obtained from their assigned $^{1}H^{N}$, ^{15}N, $^{13}C^{\alpha}$, and $^{13}C^{\beta}$ chemical shifts using the program SSP (Marsh et al., 2006), is shown in the middle. Scores of +1, 0, and −1 correspond to helices, random coils, and strands, respectively. The Random Coil Index profiles for the populations A and B of $PrgK_{19–92}$, obtained from their assigned $^{1}H^{N}$, ^{15}N, $^{13}C^{\alpha}$, and $^{13}C^{\beta}$ chemical shifts using the RCI server (Berjanskii and Wishart, 2007), are shown at the bottom. Residues 72–84 are less disordered in population A than in population B.

(D) Crystal structure of $PrgK_{19–92}$, in ribbon representation, with corresponding sequence numbering shown. Secondary structure elements are labeled as in Figure S1A, and blue to red rainbow coloring indicates N- to C-terminal directionality (see Table 2 for statistics).

(E) Close-up view of the linker region (in red) interaction with D1 (green). The composite 2Fo-Fc omit map (0.05% atoms omitted, generated by Phenix) is shown, contoured at 1 σ around residues 75–82. Residues that form hydrophobic interactions between D1 and the linker are shown as sticks.

See also Figure S5.

protein PrgK, from the prototypical *Salmonella* SPI-1 T3SS injectisome. We demonstrate that its C-terminal TM helix is not essential for injectisome assembly/effector secretion and report the crystallographic and NMR structures of its two globular domains in isolation. Using our previously developed molecular modeling method combining atomic structures of individual domains, EM maps, and symmetry, we have obtained a model of the PrgK periplasmic ring. Further analysis in the context of its binding partner PrgH provides a starting point for understanding the intimate molecular interaction between these two ring-forming proteins. Finally, we propose that the linker region between the two globular ring-building domains of PrgK may play a regulatory role in oligomerization, by promoting an intermolecular, domain-swapped disposition of D1 and D2 that stabilizes the 24-mer ring complex.

Previous studies have shown that coexpression of PrgK and PrgH leads to the spontaneous formation of the inner-membrane ring structures. In contrast, expression of PrgK or PrgH alone forms oligomers, but lacks the ring-like conformation observed in the fully assembled injectisome (Kimbrough and Miller, 2000). In this light, the data reported here suggest a molecular mechanism for the assembly of the PrgH-PrgK rings. We propose that PrgK can adopt two conformations: an assembly-incompetent conformation with D1 sequestering the linker and an assembly-competent conformation where the linker promotes oligomerization. This conformation is likely stabilized by the insertion of a PrgH molecule in between two adjacent PrgK

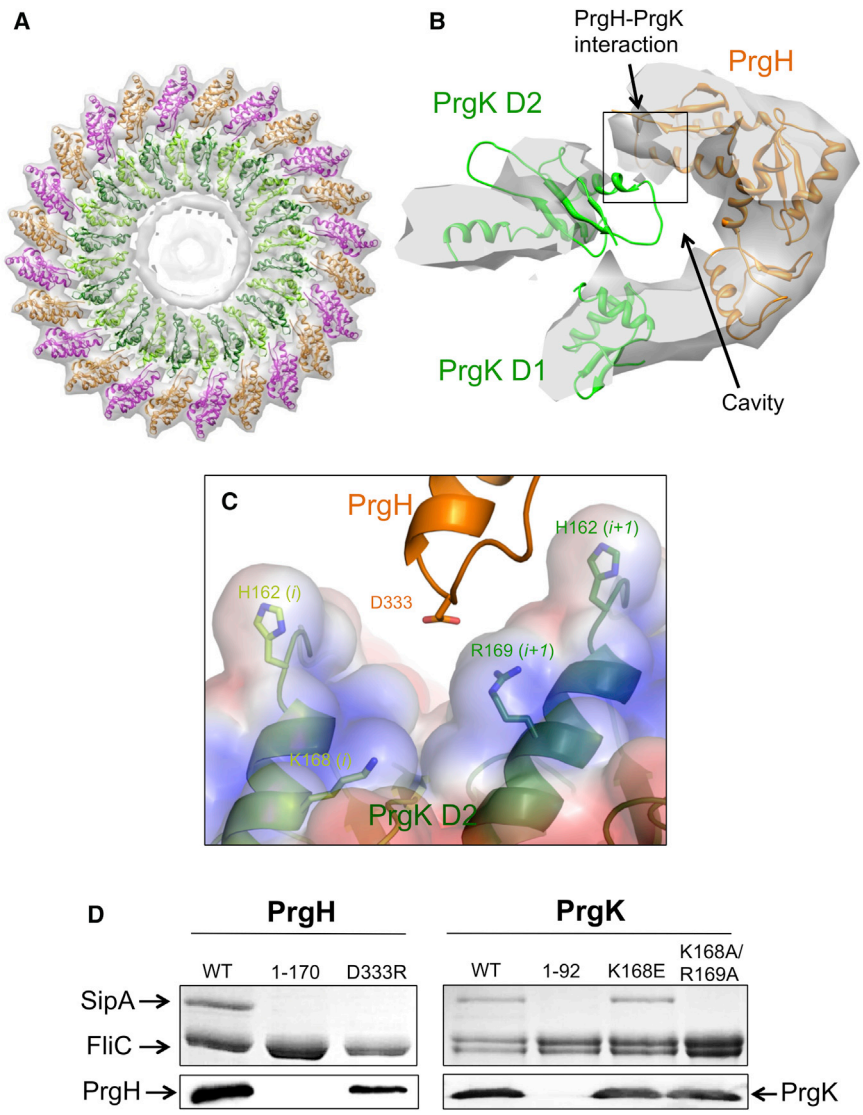

Figure 7. Structural Model of the PrgH-PrgK Complex

(A) Ribbon representation of the lowest energy model for the PrgH-PrgK 48-mer model, in the EM density of the map used for the Rosetta modeling (EM Data Bank ID: 1875). Adjacent subunits of PrgH are colored pink and orange, and adjacent subunits of PrgK are in green and yellow.

(B) Side view of a single PrgH, PrgK D1 and PrgK D2 subunit, in orange and green, respectively, with the EM density in gray (contour level = 0.24). The location of the proposed PrgH-PrgK interaction, as well as the large cavity between the two molecules, is indicated.

(C) Close-up view of the PrgH-PrgK interface. Adjacent PrgK D2 molecules are in green and yellow, respectively, while the PrgH molecule is in orange. The residues that participate in the PrgH-PrgK interaction are indicated; a negative-charged residue on PrgH, Asp 333, docks in a positively charged pocket formed by His 162 and Lys 168 from one PrgK subunit (*i*) and Arg 169 and His 162 from the adjacent PrgK subunit (*i+1*). A surface representation of the PrgK dimer, colored according to the surface charge calculated using APBS (Baker et al., 2001), is shown.

(D) SDS-PAGE gel of proteins secreted by *S. typhimurium* strains containing mutations of PrgH or PrgK. FliC is used as a loading control. The western blots for PrgH (left) or PrgK (right) from isolated membrane fractions of the corresponding samples are shown below. In PrgH, mutation of Asp 333 abrogates secretion, while in PrgK mutation of Lys 168 to Glu has no phenotype, but secretion is abrogated when both Lys 168 and Arg 169 are mutated to Ala. These results support the essential role of the proposed PrgH-PrgK interface in T3SS assembly. We note that protein levels are decreased for all mutants compared with WT, likely caused by increased protein turnover in the absence of complex formation (Schraidt and Marlovits, 2011).

See also Figure S6 and Table S1.

molecules, which would explain why PrgK or PrgH alone do not spontaneously form ring-like oligomers. Propagation of this ring-initiation step leads to the formation of a stable PrgH-PrgK 24-mer ring pair (Figure 8). We argue that such a coordinated oligomerization of these two conserved luer lock rings would be essential to allow their formation only upon encompassing the several inner-membrane spanning export apparatus proteins that they are presumed to contain (Wagner et al., 2010).

We acknowledge that this proposed mechanism is derived largely from the biochemical and structural behavior of a soluble, monomeric fragment of PrgK and may therefore not reflect the behavior of the full-length membrane-embedded protein in vivo. However, the correlation between the impact of PrgK mutations in vitro and in vivo, as well as the ability to isolate a PrgH/K complex (Kimbrough and Miller, 2000), supports the validity of the proposed model. Although perhaps intuitively sensible that a large complex such as the PrgK-PrgH oligomer would assemble in a coordinated, step-wise manner, additional experimental validation, such as the isolation and molecular characterization of assembly intermediates, will be required to confirm the model proposed in Figure 8.

A second aspect of this study is the proposed model for the PrgH-PrgK interaction from our Rosetta-based analysis. Perhaps surprising is the somewhat limited nature of this interface that, although bolstered by stoichiometry, suggests additional functionalities, such as the lipidated and/or membrane-spanning regions of PrgH and PrgK, may also play a role. Alternatively, the presence of peptidoglycan, cytoskeleton, or other structural components in the periplasm may also act in stabilizing the complex in the membrane environment. Further, both the EM map density and our symmetry modeling suggest the presence of a large cavity between PrgH and PrgK (Figure 7), with few interactions occurring in the periplasmic region (although it is possible that in situ this cavity is occupied by other components of the injectisome that perhaps are lost during needle complex purification in the EM analysis). This cavity could

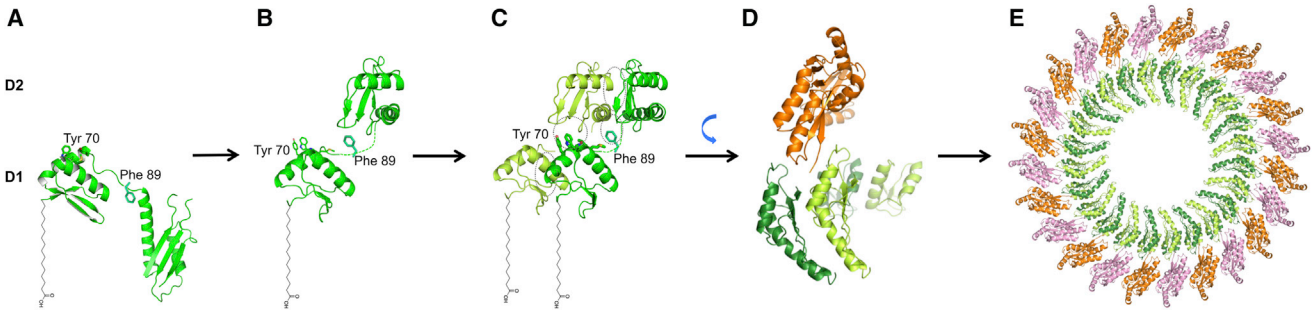

Figure 8. Molecular Model for the Assembly of the PrgH-PrgK Ring

(A) We propose that initially PrgK exists in a monomeric state, while localized in the inner membrane via nature of the N-terminal lipidation site and the C-terminal TM helix. D1 interacts with the linker, preventing oligomerization. The C-terminal TM helix, which is not essential for assembly (as shown in Figure 1C) is omitted for clarity.

(B) The linker then dissociates from D1, exposing the Tyr 70-containing hydrophobic pocket, as well as Phe 89.

(C) PrgK then recruits adjacent molecules via a range of intermolecular interactions involving both domains and the linker region, indicated by dotted black circles.

(D) PrgH molecules insert in the pocket formed by two adjacent PrgK molecules, forming a heterotrimeric intermediate.

(E) PrgH-PrgK heterotrimers further oligomerize to obtain an assembled PrgH-PrgK complex.

allow for a degree of structural plasticity in the basal body, as observed recently in situ for the *Yersinia* T3SS (Kudryashev et al., 2013). The presence of a cavity into which solvent can diffuse between PrgH and PrgK could also have favorable implications in the design of T3SS assembly inhibitors.

In conclusion, in this study, we have obtained the structures of isolated domains of PrgK and used interaction studies and computational methods to propose a structural model for the PrgH-PrgK 48-mer periplasmic rings. This provides insights into the interaction between PrgH and PrgK. We also report biochemical, structural, and functional data suggesting a stepwise assembly for the PrgH-PrgK complex, promoted by structural rearrangement in PrgK. While integrative structural biology approaches enable the piecing together of the architecture of large macromolecular assemblies, the addition of a temporal dimension, including assembly, disassembly, and/or functional changes, such as that probed here, is an important further element toward understanding and targeting complex nanomachines such as the T3SS at the molecular level.

EXPERIMENTAL PROCEDURES

Protein Expression and Purification

All constructs were cloned in a pET28a plasmid (Novagen), with an N-terminal His_{10}-tag fusion followed by a thrombin cleavage site. Plasmids were transformed into *E. coli* BL21(DE3) cells, and transformants were grown to log phase at 37°C. Expression was induced with 1 mM isopropyl β-D-1-thiogalactopyranoside at 20°C for 16 hr. Harvested cells were resuspended in lysis buffer (50 mM HEPES [pH 8.0], 150 mM NaCl) with protease inhibitors (Roche). Cells were lysed by sonication. Clarified lysate was run through Zn-chelating sepharose, and the proteins were eluted with 500 mM imidazole. The His-tag was cleaved with Thrombin (Roche), and proteins were further purified by gel filtration with a Superdex 75 column (GE Healthcare).

For NMR experiments, ^{15}N- and ^{15}N, ^{13}C-labeled proteins were expressed in *E. coli* BL21(DE3) in M9 minimal media supplemented with 1 g/l $^{15}NH_4Cl$ and 2.5 g/l ^{13}C-labeled glucose. The proteins were purified as above.

NMR Spectra Acquisition, Assignment, and Structure Determination

For all NMR experiments, protein samples were dialyzed into 50 mM HEPES (pH 6.8), 10% D_2O, and concentrated to ~0.5–1 mM. Standard 2D and 3D spectra for backbone and side-chain assignments were collected using either a 600 or 850 MHz Brucker Avance III spectrometer, equipped with TCI cryoprobe. All spectra were processed using NMRPipe (Delaglio et al., 1995) and analyzed with SPARKY (T.D. Goddard and D.G. Kneller, University of California, San Francisco) (see Supplemental Experimental Procedures for details).

Crystallization and X-Ray Crystallographic Structure Determination

Crystals of $PrgK_{98–200}$ and $PrgK_{19–92}$ were obtained in 100 mM sodium acetate (pH 5.5), 20% polyethylene glycol (PEG) 6000, 50 mM NaCl, 50 mM $MgCl_2$, and 80 mM phosphate buffer (pH 4.0), 20 mM Tris pH 7.0, 25% PEG 300, 20 mM MgCl2, 20 mM NaCl, respectively, by vapor diffusion, using the sitting drop method. X-ray diffraction data were collected at the Canadian Light Source beamline 08B1-1. Phases were obtained by molecular replacement with the program Phaser (McCoy et al., 2007). The $PrgK_{98–200}$ structure was refined to 2.65 Å resolution and the $PrgK_{19–92}$ to 3.2 Å resolution (Table 2; see Supplemental Experimental Procedures for details).

EM-Guided Symmetrical Modeling

Ring modeling for PrgK D1 and PrgK D2 was performed as described previously (Bergeron et al., 2013; see Supplemental Experimental Procedures for details).

For the PrgK D1-D2-PrgH model, individual lowest energy ring models of PrgK D1, PrgK D2, and PrgH were combined into a single coordinate file and used to generate the input for the phase II all atom refinement procedure (see Supplemental Experimental Procedures for details).

In Vivo Assays

Salmonella typhimurium LT2 strains containing a deletion of the *prgH* or *prgK* gene were complemented with plasmids containing the corresponding gene or mutants, all with a C-terminal 6xHis tag, which does not affect T3SS function (Schraidt et al., 2010), and effector protein secretion was monitored as described previously (Kimbrough and Miller, 2000). Needle complexes were purified as described previously (Bergeron et al., 2013; Kubori et al., 1998; Schraidt et al., 2010).

Electron Microscopy

Samples of $PrgK_{82–200}$ were diluted to ~1 mg/ml in 50 mM HEPES (pH 7.0), 150 mM NaCl. Samples of purified needle complex particles were diluted to ~0.2 mg/ml in 10 mM Tris (pH 8.0), 500 mM NaCl, 5 mM EDTA, and 10 mM lauryldimethylamine oxide. All samples were applied on glow-discharged carbon grids and stained using 0.75% uranyl formate. Images were collected on a Technai G2 transmission electron microscope (FEI) operating at 200 kV and equipped with a high-speed AMT 2K side-mount CCD camera.

ACCESSION NUMBERS

The atomic coordinates for the various structures have been deposited in the PDB ID (2MKY, 4OYC, and 4W4M). The lowest all-atom energy PrgH-PrgK Rosetta model has been deposited in the PDB (3J6D).

SUPPLEMENTAL INFORMATION

Supplemental Information includes Supplemental Experimental Procedures, six figures, and one table and can be found with this article online at http://dx.doi.org/10.1016/j.str.2014.10.021.

AUTHOR CONTRIBUTIONS

J.R.C.B. cloned, expressed, and purified all proteins. J.R.C.B. crystallized and solved the crystal structures, with help from L.J.W. for the refinement. J.R.C.B. collected all NMR data with help from M.O. and analyzed them with help from S.D. and L.P.M. J.R.C.B. performed the ITC and circular dichroism experiments with help from L.J.W. J.R.C.B. performed the modeling experiments with N.G.S. and D.B. E.L. and G.A.W. performed the DLS and DSF experiments, respectively. J.R.C.B. performed all in vivo and EM assays with help from A.H.C. J.R.C.B. and N.C.J.S. wrote the manuscript, with comments from all coauthors.

ACKNOWLEDGMENTS

We thank Samuel Miller for providing the *S. typhimurium prgK*- and *fliC/prgK*-deletion strains. We are also grateful to Kelvin Lau, Bradford Ross, Gerd Prenha, Matthew Solomonson, and Fred Rosell for technical advice. X-ray diffraction data were collected at beamline 08B1-1 at the Canadian Light Source, which is supported by the Natural Sciences and Engineering Research Council of Canada, the National Research Council Canada, the Canadian Institutes of Health Research, the Province of Saskatchewan, Western Economic Diversification Canada, and the University of Saskatchewan. Instrument support was provided by the Canada Foundation for Innovation, the British Columbia Knowledge Development Fund, the UBC Blusson Fund, and the Michael Smith Foundation for Health Research. N.G.S. acknowledges funding by the Intramural Research Program of the National Institute of Diabetes and Digestive and Kidney Diseases, NIH. J.R.C.B. is a MSFHR postdoctoral fellow. N.C.J.S. is a Canada Research Chair Tier 1 in Antibiotic Discovery. This work was supported by operating grants from the Canadian Institute of Health Research and HHMI International Scholar Program (to N.C.J.S.).

Received: May 17, 2014
Revised: October 13, 2014
Accepted: October 17, 2014
Published: December 18, 2014

REFERENCES

Alber, F., Förster, F., Korkin, D., Topf, M., and Sali, A. (2008). Integrating diverse data for structure determination of macromolecular assemblies. Annu. Rev. Biochem. *77*, 443–477.

Allaoui, A., Sansonetti, P.J., and Parsot, C. (1992). MxiJ, a lipoprotein involved in secretion of Shigella Ipa invasins, is homologous to YscJ, a secretion factor of the Yersinia Yop proteins. J. Bacteriol. *174*, 7661–7669.

Baker, N.A., Sept, D., Joseph, S., Holst, M.J., and McCammon, J.A. (2001). Electrostatics of nanosystems: application to microtubules and the ribosome. Proc. Natl. Acad. Sci. USA *98*, 10037–10041.

Bergeron, J.R., Worrall, L.J., Sgourakis, N.G., DiMaio, F., Pfuetzner, R.A., Felise, H.B., Vuckovic, M., Yu, A.C., Miller, S.I., Baker, D., and Strynadka, N.C. (2013). A refined model of the prototypical Salmonella SPI-1 T3SS basal body reveals the molecular basis for its assembly. PLoS Pathog. *9*, e1003307.

Berjanskii, M.V., and Wishart, D.S. (2007). The RCI server: rapid and accurate calculation of protein flexibility using chemical shifts. Nucleic Acids Res. *35*, W531–W537.

Büttner, D. (2012). Protein export according to schedule: architecture, assembly, and regulation of type III secretion systems from plant- and animal-pathogenic bacteria. Microbiol. Mol. Biol. Rev. *76*, 262–310.

Coburn, B., Grassl, G.A., and Finlay, B.B. (2007a). Salmonella, the host and disease: a brief review. Immunol. Cell Biol. *85*, 112–118.

Coburn, B., Sekirov, I., and Finlay, B.B. (2007b). Type III secretion systems and disease. Clin. Microbiol. Rev. *20*, 535–549.

Crago, A.M., and Koronakis, V. (1998). Salmonella InvG forms a ring-like multimer that requires the InvH lipoprotein for outer membrane localization. Mol. Microbiol. *30*, 47–56.

Crepin, V.F., Prasannan, S., Shaw, R.K., Wilson, R.K., Creasey, E., Abe, C.M., Knutton, S., Frankel, G., and Matthews, S. (2005). Structural and functional studies of the enteropathogenic Escherichia coli type III needle complex protein EscJ. Mol. Microbiol. *55*, 1658–1670.

de Jong, H.K., Parry, C.M., van der Poll, T., and Wiersinga, W.J. (2012). Host-pathogen interaction in invasive Salmonellosis. PLoS Pathog. *8*, e1002933.

Delaglio, F., Grzesiek, S., Vuister, G.W., Zhu, G., Pfeifer, J., and Bax, A. (1995). NMRPipe: a multidimensional spectral processing system based on UNIX pipes. J. Biomol. NMR *6*, 277–293.

Demers, J.P., Sgourakis, N.G., Gupta, R., Loquet, A., Giller, K., Riedel, D., Laube, B., Kolbe, M., Baker, D., Becker, S., and Lange, A. (2013). The common structural architecture of Shigella flexneri and Salmonella typhimurium type three secretion needles. PLoS Pathog. *9*, e1003245.

Dohlich, K., Zumsteg, A.B., Goosmann, C., and Kolbe, M. (2014). A substrate-fusion protein is trapped inside the Type III Secretion System channel in Shigella flexneri. PLoS Pathog. *10*, e1003881.

Haraga, A., Ohlson, M.B., and Miller, S.I. (2008). Salmonellae interplay with host cells. Nat. Rev. Microbiol. *6*, 53–66.

Juncker, A.S., Willenbrock, H., Von Heijne, G., Brunak, S., Nielsen, H., and Krogh, A. (2003). Prediction of lipoprotein signal peptides in Gram-negative bacteria. Protein Sci. *12*, 1652–1662.

Keyser, P., Elofsson, M., Rosell, S., and Wolf-Watz, H. (2008). Virulence blockers as alternatives to antibiotics: type III secretion inhibitors against Gram-negative bacteria. J. Intern. Med. *264*, 17–29.

Kimbrough, T.G., and Miller, S.I. (2000). Contribution of Salmonella typhimurium type III secretion components to needle complex formation. Proc. Natl. Acad. Sci. USA *97*, 11008–11013.

Kline, T., Felise, H.B., Sanowar, S., and Miller, S.I. (2012). The type III secretion system as a source of novel antibacterial drug targets. Curr. Drug Targets *13*, 338–351.

Kosarewicz, A., Königsmaier, L., and Marlovits, T.C. (2012). The blueprint of the type-3 injectisome. Philos. Trans. R. Soc. Lond. B Biol. Sci. *367*, 1140–1154.

Kubori, T., Matsushima, Y., Nakamura, D., Uralil, J., Lara-Tejero, M., Sukhan, A., Galán, J.E., and Aizawa, S.I. (1998). Supramolecular structure of the Salmonella typhimurium type III protein secretion system. Science *280*, 602–605.

Kudryashev, M., Stenta, M., Schmelz, S., Amstutz, M., Wiesand, U., Castaño-Díez, D., Degiacomi, M.T., Münnich, S., Bleck, C.K., Kowal, J., et al. (2013). In situ structural analysis of the Yersinia enterocolitica injectisome. eLife *2*, e00792.

Lunelli, M., Hurwitz, R., Lambers, J., and Kolbe, M. (2011). Crystal structure of PrgI-SipD: insight into a secretion competent state of the type three secretion system needle tip and its interaction with host ligands. PLoS Pathog. *7*, e1002163.

Marlovits, T.C., Kubori, T., Sukhan, A., Thomas, D.R., Galán, J.E., and Unger, V.M. (2004). Structural insights into the assembly of the type III secretion needle complex. Science *306*, 1040–1042.

Marsh, J.A., Singh, V.K., Jia, Z., and Forman-Kay, J.D. (2006). Sensitivity of secondary structure propensities to sequence differences between alpha- and gamma-synuclein: implications for fibrillation. Protein Sci. *15*, 2795–2804.

Marshall, N.C., and Finlay, B.B. (2014). Targeting the type III secretion system to treat bacterial infections. Expert Opin. Ther. Targets *18*, 137–152.

McCoy, A.J., Grosse-Kunstleve, R.W., Adams, P.D., Winn, M.D., Storoni, L.C., and Read, R.J. (2007). Phaser crystallographic software. J. Appl. Cryst. *40*, 658–674.

Okon, M., Moraes, T.F., Lario, P.I., Creagh, A.L., Haynes, C.A., Strynadka, N.C., and McIntosh, L.P. (2008). Structural characterization of the type-III pilot-secretin complex from Shigella flexneri. Structure *16*, 1544–1554.

Radics, J., Konigsmaier, L., and Marlovits, T.C. (2014). Structure of a pathogenic type 3 secretion system in action. Nat. Struct. Mol. Biol. *21*, 82–87.

Sanowar, S., Singh, P., Pfuetzner, R.A., Andre, I., Zheng, H., Spreter, T., Strynadka, N.C., Gonen, T., Baker, D., Goodlett, D.R., et al. (2009). Interactions of the transmembrane polymeric rings of the Salmonella enterica serovar Typhimurium type III secretion system. MBiol. *1*, e00158-10.

Schraidt, O., and Marlovits, T.C. (2011). Three-dimensional model of Salmonella's needle complex at subnanometer resolution. Science *331*, 1192–1195.

Schraidt, O., Lefebre, M.D., Brunner, M.J., Schmied, W.H., Schmidt, A., Radics, J., Mechtler, K., Galán, J.E., and Marlovits, T.C. (2010). Topology and organization of the Salmonella typhimurium type III secretion needle complex components. PLoS Pathog. *6*, e1000824.

Sekiya, K., Ohishi, M., Ogino, T., Tamano, K., Sasakawa, C., and Abe, A. (2001). Supermolecular structure of the enteropathogenic Escherichia coli type III secretion system and its direct interaction with the EspA-sheath-like structure. Proc. Natl. Acad. Sci. USA *98*, 11638–11643.

Spreter, T., Yip, C.K., Sanowar, S., André, I., Kimbrough, T.G., Vuckovic, M., Pfuetzner, R.A., Deng, W., Yu, A.C., Finlay, B.B., et al. (2009). A conserved structural motif mediates formation of the periplasmic rings in the type III secretion system. Nat. Struct. Mol. Biol. *16*, 468–476.

Troisfontaines, P., and Cornelis, G.R. (2005). Type III secretion: more systems than you think. Physiology (Bethesda) *20*, 326–339.

Wagner, S., Königsmaier, L., Lara-Tejero, M., Lefebre, M., Marlovits, T.C., and Galán, J.E. (2010). Organization and coordinated assembly of the type III secretion export apparatus. Proc. Natl. Acad. Sci. USA *107*, 17745–17750.

Wang, Y., Ouellette, A.N., Egan, C.W., Rathinavelan, T., Im, W., and De Guzman, R.N. (2007). Differences in the electrostatic surfaces of the type III secretion needle proteins PrgI, BsaL, and MxiH. J. Mol. Biol. *371*, 1304–1314.

Worrall, L.J., Lameignere, E., and Strynadka, N.C. (2011). Structural overview of the bacterial injectisome. Curr. Opin. Microbiol. *14*, 3–8.

Yip, C.K., Kimbrough, T.G., Felise, H.B., Vuckovic, M., Thomas, N.A., Pfuetzner, R.A., Frey, E.A., Finlay, B.B., Miller, S.I., and Strynadka, N.C. (2005). Structural characterization of the molecular platform for type III secretion system assembly. Nature *435*, 702–707.

